

# The Welding Metallurgy of HASTELLOY Alloys C-4, C-22, and C-276

M. J. CIESLAK, T. J. HEADLEY, and A. D. ROMIG, Jr.

The welding metallurgy (solidification and solid state transformations) of HASTELLOY\* Alloys C-4, C-22, and C-276 has been determined. Vareststraint hot-cracking tests performed on commercial alloys revealed a weldability ranking as follows: C-4 > C-22 > C-276. All alloys would be expected to have good weldability, with Alloy C-4 having a very low hot-cracking tendency, comparable to 304L stainless steel. Microstructures of gas-tungsten-arc welds of these alloys have been characterized by scanning electron microscopy and analytical electron microscopy. Intermetallic secondary solidification constituents have been found associated with weld metal hot cracks in Alloys C-276 and C-22. In Alloy C-276, this constituent is a combination of  $P$  and  $\mu$  phases, and in Alloy C-22, this constituent is composed of  $\sigma$ ,  $P$ , and  $\mu$  phases. With phase composition data obtained by AEM techniques and available ternary (Ni-Cr-Mo) phase diagrams, an equivalent chemistry model is proposed to account for the microstructures observed in each alloy's weld metal.

## I. INTRODUCTION

HASTELLOY Alloys C-4, C-22, and C-276 are highly corrosion-resistant nickel-base alloys derived from the Ni-Cr-Mo ternary system. In addition to the expected impurities (Table I), Alloy C-4 has an intentional Ti alloying addition, and Alloys C-22 and C-276 have W and Fe as additional alloying components. These materials are nominally single-phase, solid-solution strengthened alloys not hardenable by conventional aging treatments.

The thermal stability of these and similar (*e.g.*, HASTELLOY S) alloys in the mill-annealed condition has been investigated in some detail.<sup>1-8</sup> Long range ordering has been observed<sup>1-4</sup> in which the disordered face-centered-cubic matrix transforms to an ordered orthorhombic superlattice (isomorphous with Pt<sub>2</sub>Mo). This phenomenon generally occurs only after at least several hundred hours in the 600 °C temperature range and hence is not important in the consideration of the fusion zone microstructure generated by cooling rates characteristic of arc welding.<sup>9</sup>

Precipitation of intermetallic phases ( $\mu$ ,  $P$ ) and carbides has also been observed.<sup>1,5-8</sup> The intermetallic compounds are the most relevant to the present study. Leonard<sup>8</sup> has shown that  $P$  phase can precipitate in Alloy C-276 within a few minutes of exposure at 875 °C. He also suggests that  $\mu$  phase is the long-time transformation product of  $P$  phase. Hodge and Kirchner<sup>6</sup> found no evidence of  $\mu$  phase formation in Alloy C-4 during isothermal heat treatments in the temperature range 650 °C to 1090 °C for times up to 100 hours. Matthews<sup>1</sup> reported that  $\mu$  phase precipitation occurs in Alloy C-4, but only after extended heat treatment ( $\geq 1000$  hours) in the 800 °C temperature regime.

Recently, Cieslak *et al.*<sup>10</sup> reported on the occurrence of topologically-close-packed phases in Alloy C-22 and Alloy C-276 weld metal. Alloy C-276 contained both the  $P$  and  $\mu$

phases. Alloy C-22 contained  $P$ ,  $\mu$ , and  $\sigma$  phases. All of these phases are possible equilibrium structures in the Ni-Cr-Mo ternary system.<sup>11,12,13</sup> Raghavan *et al.*<sup>13</sup> observed that  $P$  and  $\sigma$  phases were present in the near-solidus (1250 °C) isothermal section of the Ni-Cr-Mo system; and  $P$ ,  $\sigma$ , and  $\mu$  phases were present in the 850 °C isothermal section. Bloom and Grant<sup>12</sup> speculated on the high temperature invariant reactions above 1250 °C in the Ni-Cr-Mo system. In the composition range of importance relative to commercial alloys, the possible equilibrium phases were liquid, austenite ( $\gamma$ ),  $P$ , and  $\sigma$ .

In this paper we report the results of hot-cracking susceptibility tests on Alloys C-4, C-22, and C-276, and the identification of the minor phases ( $P$ ,  $\sigma$ ,  $\mu$ , or MC carbide) in the solidified weld microstructures. An equivalent chemistry model is then developed which accounts for the second phases observed in terms of a secondary solidification constituent in each alloy plus subsequent solid-state transformation reactions in Alloys C-22 and C-276.

## II. EXPERIMENTAL PROCEDURE

The chemical analyses of the alloys studied are given in Table I. All alloys were sheet products, approximately 0.3 cm thick and all were in the mill-annealed condition prior to welding. All welding was done using the auto-genous (no filler metal added) gas-tungsten-arc (GTA) process. The welding parameters used were 100 A, direct current, electrode negative, at 13.5 V (machine voltage), and a travel speed of 20 cm/min.

The hot-cracking susceptibility was quantified with the Vareststraint test.<sup>14,15</sup> Earlier work<sup>16,17</sup> has indicated that this test is a reliable means for differentiating the hot-cracking susceptibility of nickel-base alloys. The Vareststraint test employs a 16.5 cm  $\times$  2.5 cm  $\times$  0.3 cm specimen supported as a cantilever beam as shown schematically in Figure 1(a). A GTA weld is made from left to right as indicated. As the weld pool passes the point marked A, a pneumatic loading system (at point F) bends the specimen to conform to the radiused die block labeled B. The arc continues without stopping to the point labeled C, where it is extinguished. From simple geometric arguments, the longitudinal aug-

\*HASTELLOY is a trademark of Cabot Corporation.

M. J. CIESLAK, Div. 1833, Process Metallurgy, T. J. HEADLEY, Div. 1822, Electron Optics and X-Ray Analysis, and A. D. ROMIG, Jr., Div. 1832, Physical Metallurgy, are with Sandia National Laboratories, P.O. Box 5800, Albuquerque, NM 87185.

Manuscript submitted January 2, 1986.

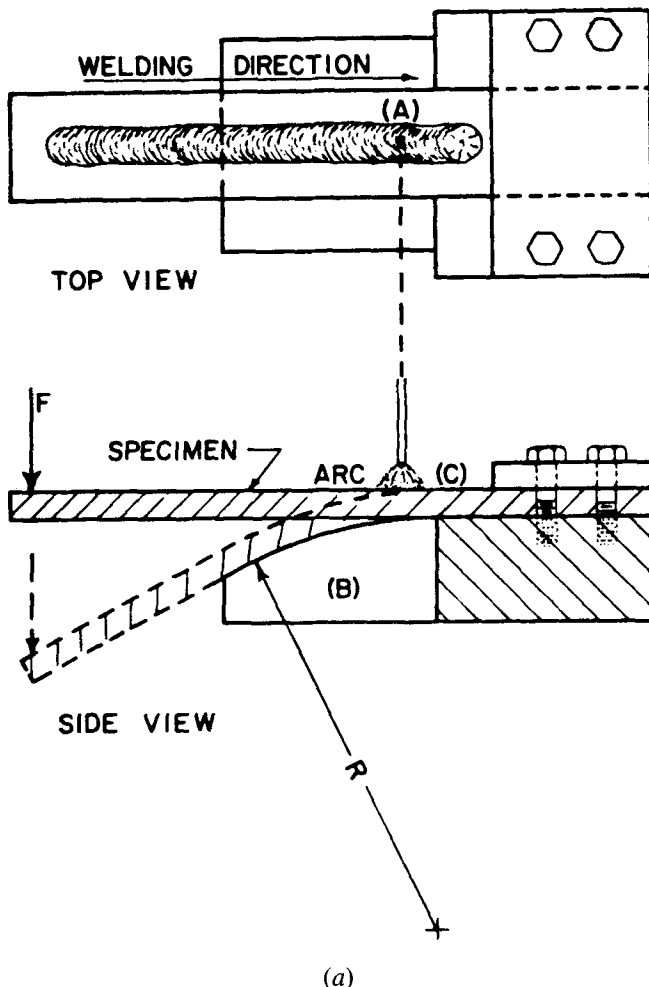
Table I. Alloy Compositions (Wt Pct)

Element	HASTELLOY	HASTELLOY	HASTELLOY
	C-4	C-22	C-276
C	0.004	0.006	0.003
Co	0.10	0.84	0.96
Cr	15.69	21.22	15.83
Fe	0.45	3.17	5.44
Mn	0.17	0.31	0.50
Mo	15.06	13.43	15.56
Ni	67.20	56.96	55.58
P	<0.005	0.010	0.014
S	<0.002	<0.002	0.002
Si	0.03	<0.02	0.03
Ti	0.23	0.03	<0.01
V	0.02	0.14	0.18
W	<0.10	3.29	3.93

mented strain,  $\epsilon$ , at the top surface of the bar can be calculated from the following relationship,

$$\epsilon \approx t/2R, \quad [1]$$

where  $t$  = specimen thickness and  $R$  = die block radius of curvature. Tests were run at various levels of augmented strain (0.8 pct to 2.5 pct) by substituting the appropriately radiused die block. Following testing, the as-welded surface of the specimens was examined under a stereomicroscope



equipped with a filar eyepiece. Fusion zone hot cracks were observed at positions shown schematically in Figure 1(b). The sum of the length of all the cracks emanating back into the fusion zone from the position of the solid/liquid interface at the instant of straining, the total crack length, is the quantitative measure of weldability determined from Vareststraint testing. The maximum crack length is the length of the longest hot crack found on a particular specimen. For alloys having similar thermal conductivities and melting temperatures, this value is proportional to the hot-cracking temperature range.<sup>15</sup> Expected scatter parameters (standard deviation/mean) in Vareststraint data are 15 pct to 20 pct.

In order to study elemental segregation associated with solidification, *in situ* water spray quenched experiments<sup>18,19</sup> were performed. Samples of each alloy were welded using the same welding parameters as those used in the Vareststraint tests. At the point where strain would normally be imposed upon the specimen, a high pressure water spray quench fixture would both decant the liquid in the weld pool and rapidly cool the dendrites which were then growing into the trailing edge of the weld. This quenching procedure minimizes the extent of solid state diffusion during normal cooling of the weld metal to room temperature and retains the pattern of elemental microsegregation associated with weld solidification.

Subsequent to welding, samples for microstructural analysis were removed from the Vareststraint test specimens as shown schematically in Figure 1(b). These samples were mounted in epoxy and polished through 0.05  $\mu\text{m}$  alumina. Microstructures were revealed with a 10 pct chromic acid electroetch. The specimens were then carbon coated and examined in a Hitachi S-520 scanning electron microscope (SEM).

Samples for electron microprobe analysis were taken from the trailing edge of the weld pool of the water-quenched specimens. These were prepared in the same manner as the microstructural analysis specimens except that care was taken to grind as little material as possible off the weld surface. Microhardness indentations were used to bracket areas for microanalysis. Prior to microanalysis, the specimen surface was repolished flat with 1  $\mu\text{m}$  diamond paste and was then carbon coated. Microanalysis was performed with a Cameca MBX electron microprobe operating at an accelerating potential of 15 kV and a beam current of approximately 20 nA.  $K_{\alpha}$  X-ray peaks were used to analyze for all elements of interest except for Mo and W, where the  $L_{\alpha}$  peaks were used. Point count data were reduced to

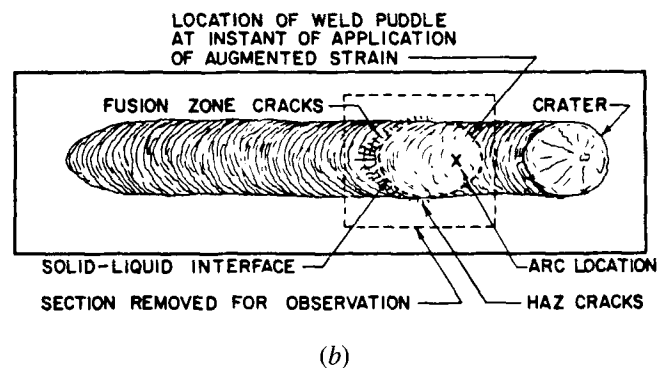


Fig. 1—(a) Schematic view of the Vareststraint test apparatus; (b) schematic top view of specimen after testing.

weight percentages with a  $\phi(\rho, Z)$  computer algorithm.<sup>20</sup> All microprobe data have a scatter of better than  $\pm 2$  pct (relative).

The samples for analytical electron microscope (AEM) analysis were sliced from weld metal of Varestraint specimens with a low-speed carbide saw and ground to a thickness of approximately 125  $\mu\text{m}$ . Standard 3 mm-diameter disks were cut from the thin sheet with a mechanical punch. Thin foils were prepared by electropolishing in a solution of 10 pct perchloric acid in methanol at approximately  $-65^\circ\text{C}$ . Following electrochemical thinning, the foils were placed in an ion mill to increase the amount of thin area and to remove any electrolyte residue. The foils were examined in a JEOL 100C AEM operated at 100 kV, equipped with a side-entry, low take-off angle X-ray detector and a Tracor Northern TN2000 multichannel analyzer.

Electron diffraction was used to identify uniquely each phase prior to X-ray microanalysis. The phases were then analyzed with a focused beam in the scanning transmission electron microscope (STEM) mode. The particles analyzed were all 0.5 to 1.0  $\mu\text{m}$  in diameter. The nominal thickness of the foil at the points of analysis was 50 to 100 nm. Under these experimental conditions, the beam scattering volume was contained entirely within the phase with no contribution from the adjacent matrix.

Phase compositions were determined from AEM X-ray data with the standardless ratio technique, where the weight fractions are related to the measured X-ray intensities by,

$$C_X/C_{\text{Ni}} = k_{X\text{Ni}}\{I_X/I_{\text{Ni}}\}, \quad [2]$$

where  $X = \text{Fe, Cr, Co, Mo, or W}$ ;  $C$  is the composition in weight percent;  $I$  is the integrated X-ray intensity; and  $k_{X\text{Ni}}$  is the Cliff-Lorimer sensitivity factor referenced to Ni. The values of the sensitivity factors,  $k_{X\text{Ni}}$ , were determined from a well-homogenized sample of Alloy C-276 with a well-known composition. The  $k_{W\text{Ni}}$  was determined for the family of  $W L_\beta$  lines. It was not possible to integrate over any individual  $W L_\beta$  X-ray line due to line overlap. However, no error is introduced into the analysis if the same integration windows are used for the experimental determination of  $k_{X\text{Ni}}$  and for the analysis of the unknown. Table II lists the sensitivity factors used in this study. The compositions of the unknowns were determined with the experimental values of  $k_{X\text{Ni}}$  in a standard data reduction routine.<sup>21</sup> X-ray absorption in these samples was not significant. At the 5 pct level of significance, the thin film criterion is violated only at a thickness exceeding 250 nm,<sup>22</sup> and foils examined in this study were typically 50 to 100 nm thick.

Differential thermal analysis (DTA) was performed on all alloys with a Dupont differential thermal analyzer. The starting condition of all DTA samples was the mill-annealed condition. Specimen weights ranged from 60 to 100 mg. A platinum standard was used for the control material.

Table II. Sensitivity Factors ( $k_{X\text{Ni}}$ )

Elemental Ratio	$k_{X\text{Ni}}$
Cr/Ni	$0.83 \pm 0.02$
Mo/Ni	$3.41 \pm 0.2$
Fe/Ni	$0.95 \pm 0.03$
$W(L_\beta)/\text{Ni}$	$9.09 \pm 0.6$
Co/Ni	$1.62 \pm 0.08$

Samples were heated at a rate of  $10^\circ\text{C}/\text{min}$  under an argon atmosphere to a temperature of  $1450^\circ\text{C}$ . At this temperature, all alloys were completely molten. Specimens were then cooled, also at a rate of  $10^\circ\text{C}/\text{min}$ , through the solidification temperature range. Primary and secondary solidification reactions on cooling were noted.

### III. RESULTS

The results of Varestraint testing are shown in Figure 2. The total crack length data indicate that Alloy C-276 has the poorest resistance to hot cracking of the three alloys and that Alloy C-4 has the best resistance to hot cracking under these test conditions. The cracking response of Alloy C-4 is similar to what would be expected of a 304L stainless steel containing 5 to 10 pct delta-ferrite, that is, a low susceptibility to fusion zone hot cracking. In general, each alloy would be expected to have good weldability when compared to other nickel base alloys such as INCONEL\*

\*INCONEL is a trademark of the INCO family of companies.

625<sup>23,24</sup> or INCONEL 718.<sup>24</sup> The maximum crack length results are shown in Figure 3. Within experimental deviation, Alloys C-276 and C-22 show similar results and both are different from Alloy C-4, which had maximum crack lengths approximately 60 pct less than the other two alloys.

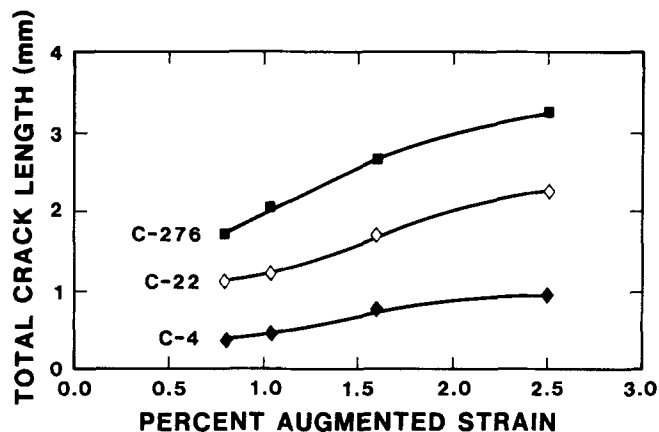


Fig. 2—Varestraint test total crack length data.

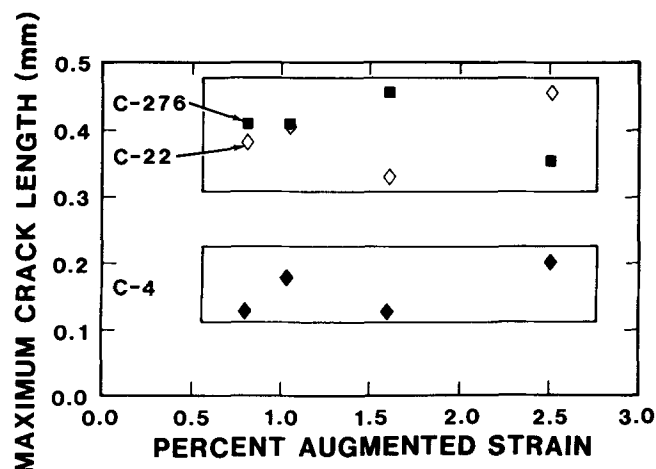
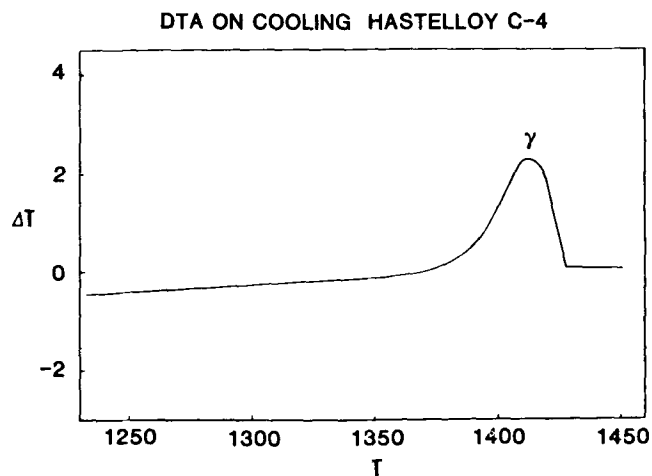
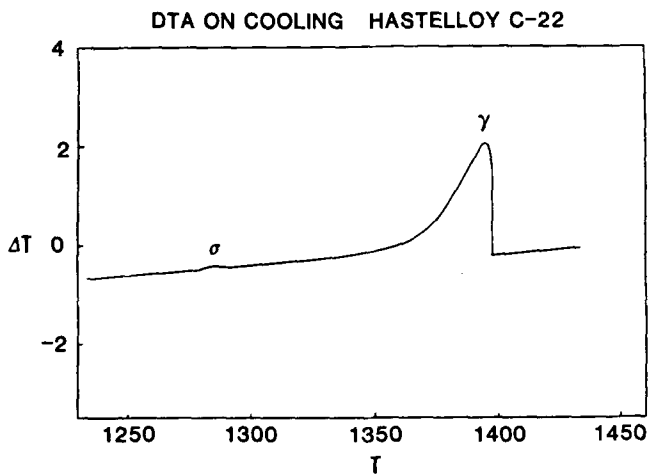


Fig. 3—Varestraint test maximum crack length data.

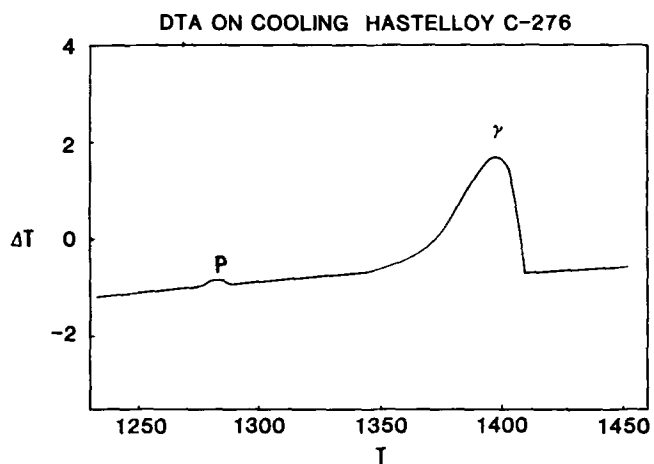
On-cooling DTA results are given in Figure 4. Figure 4(a) shows a single exothermic peak corresponding to the crystallization of austenite ( $\gamma$ ) from the melt of Alloy C-4. No other peak was discernible for Alloy C-4, suggesting a simple, single-phase solidification sequence for



(a)



(b)



(c)

Fig. 4—(a) DTA profile on cooling for Alloy C-4; (b) DTA profile on cooling for Alloy C-22; (c) DTA profile on cooling for Alloy C-276; all temperatures in °C.

this alloy. Figure 4(b) shows the DTA results for Alloy C-22. In addition to the large  $\gamma$  exotherm, there is a second small peak at approximately 1285 °C. As will be described later, this peak corresponds to the secondary solidification of  $\sigma$  phase. Figure 4(c) shows the DTA results for Alloy C-276. In a similar manner to Alloy C-22, this alloy has both a peak corresponding to primary  $\gamma$  solidification and a peak, larger than in the C-22 case, at approximately 1285 °C corresponding to a secondary solidification constituent, identified later as  $P$  phase.

Figure 5 shows the microstructure of a water quenched specimen of Alloy C-276. This microstructure was typical of all alloys investigated with the water-quench technique. In the present case, the solidification and welding directions are from left to right in the figure. A series of parallel-growing dendrites can be seen in the center of the figure, the tips of which were growing into the trailing edge of the weld pool at the instant of quenching. Microprobe profiles were taken transverse to the primary growth direction, as indicated by the arrows. The results of these analyses are shown in Figures 6 through 8. A portion of the microprobe profile obtained from each specimen is given, beginning at a particular dendrite core (DC) and terminating at the interdendritic (ID) region between adjacent dendrites. What can be seen as common to all three alloys is that the dendrite cores are enriched in Ni and depleted in Mo relative to the interdendritic regions. This implies that solidification will occur along a path of increasing Mo concentration at the expense of Ni. In addition, it can be observed that there is effectively no Cr segregation associated with solidification in any of the alloys examined.

The segregation profiles of the minor alloying elements (Fe, W, Ti) are somewhat less distinct than those of the major elements. Amongst considerable scatter, segregation of Fe to dendrite cores and Ti to interdendritic volumes in Alloy C-4 is shown in Figure 6(b). The Ti segregation associated with solidification of Alloy C-4 can be seen with greater ease in Figures 9(a) and 9(b). Figure 9(a) is a back-scattered electron image taken in the microprobe of Alloy C-4 weld metal. The interdendritic regions are the light-appearing areas, which have a higher average atomic

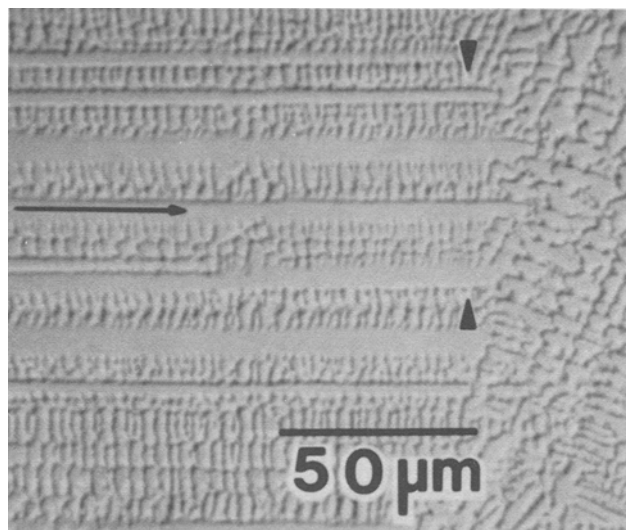


Fig. 5—Water-quenched specimen of Alloy C-276.

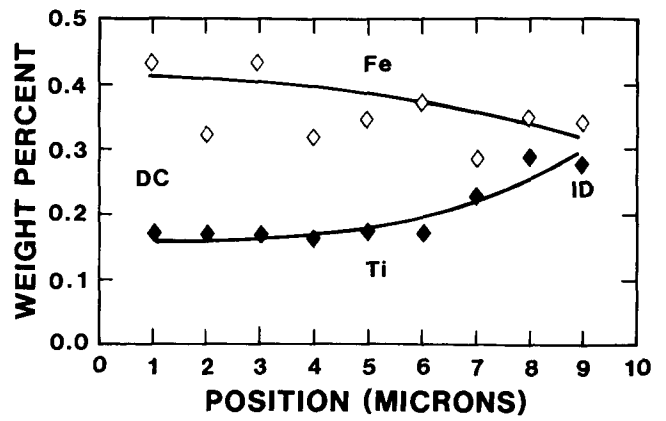
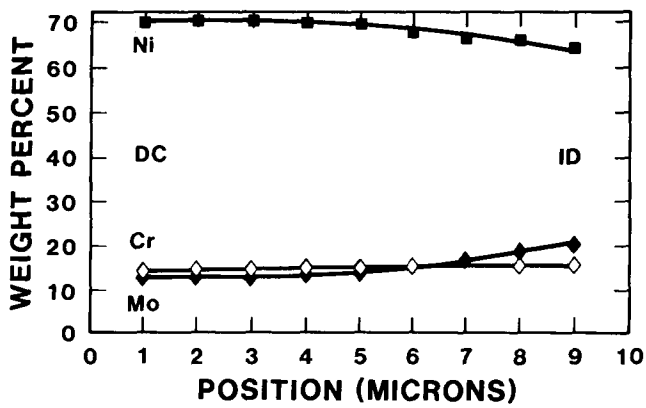


Fig. 6—(a) Major element segregation pattern in Alloy C-4 water-quenched weld metal; (b) minor element segregation pattern along the same profile as (a).

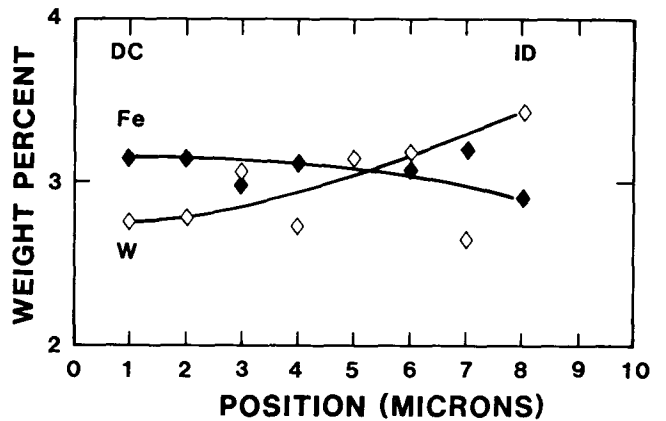
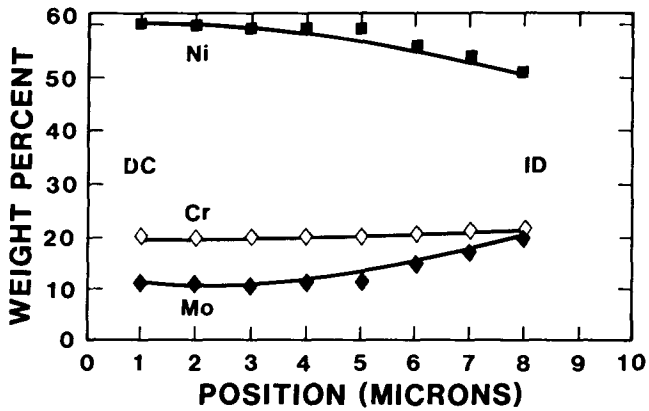


Fig. 7—(a) Major element segregation pattern in Alloy C-22 water-quenched weld metal; (b) minor element segregation pattern along the same profile as (a).

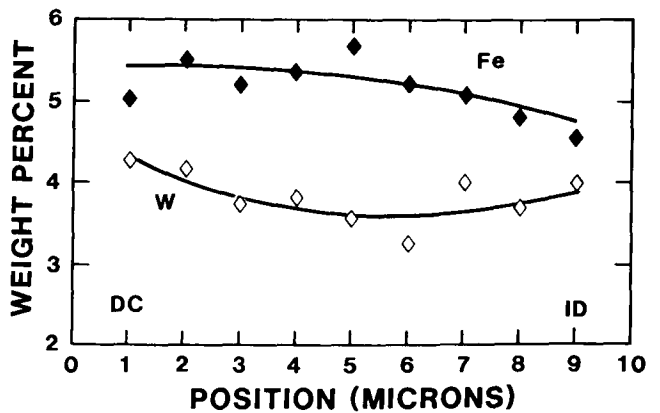
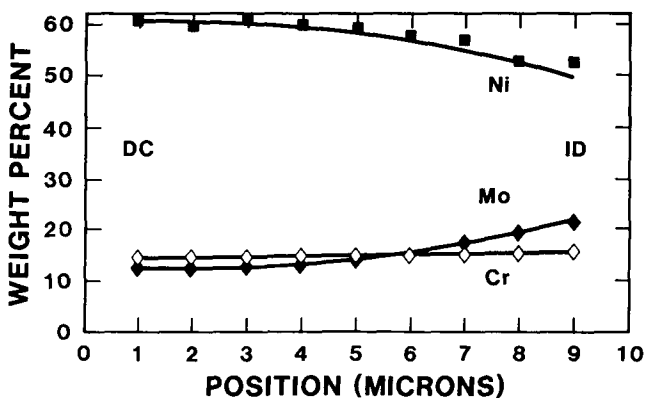
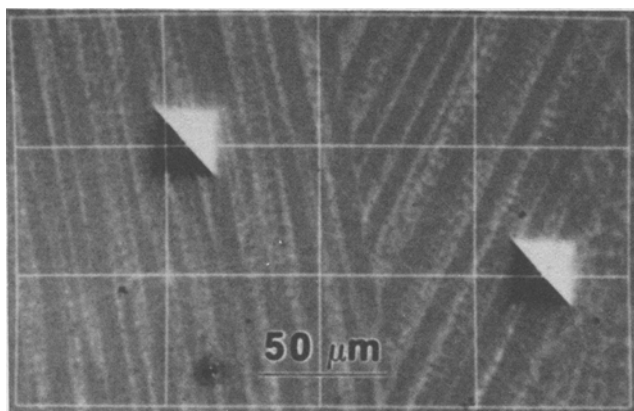
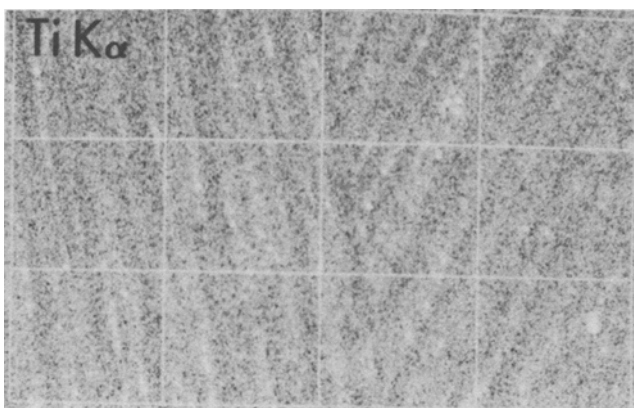


Fig. 8—(a) Major element segregation pattern in Alloy C-276 water-quenched weld metal; (b) minor element segregation pattern along the same profile as (a).



(a)



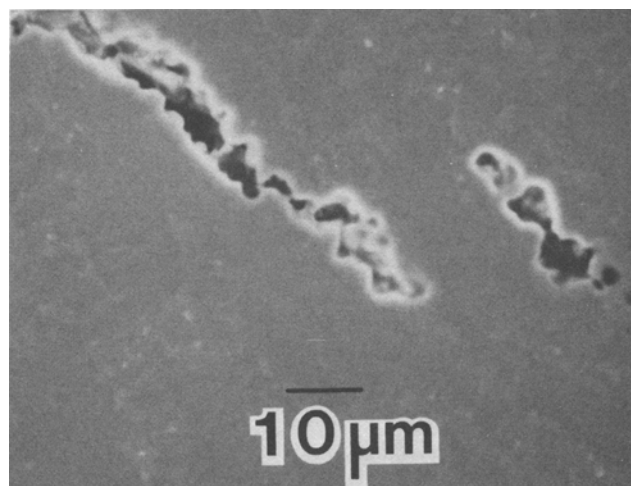
(b)

Fig. 9—(a) Backscattered electron image of Alloy C-4 weld metal, un-etched; (b)  $Ti K_{\alpha}$  X-ray map of the same region.

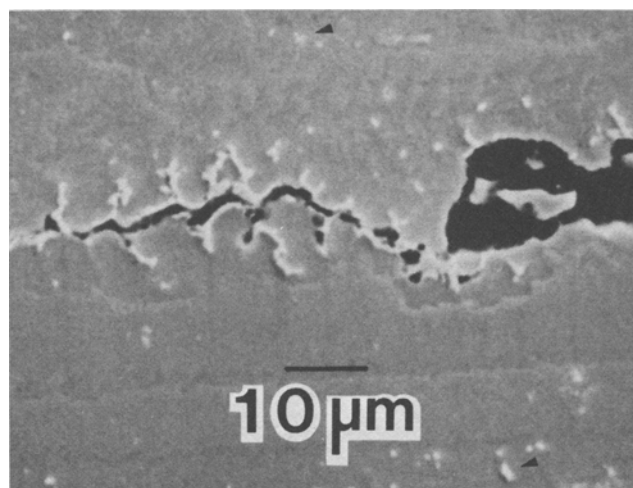
number (higher Mo content) than the dendrite core regions. Figure 9(b) is the corresponding X-ray map of  $Ti K_{\alpha}$  radiation which clearly shows the pattern of Ti segregation to interdendritic volumes. In both Alloys C-22 and C-276, Fe appears to segregate to dendrite core regions (Figures 7(b), 8(b)) in a manner similar to Ni. The segregation of W is more difficult to discern against the data scatter, and no distinct pattern was obvious.

Microstructures from the Varestraint test specimens are shown in Figure 10. Figure 10(a) is a SEM micrograph of a hot-cracked region from Alloy C-4. Note the absence of a secondary constituent in the vicinity of the cracks. Figures 10(b) and 10(c) are SEM micrographs of hot-cracked regions in alloys C-22 and C-276, respectively. Note in both cases the presence of a secondary constituent associated with the hot cracks. This kind of microstructure is typical<sup>25,26,27</sup> of weld metal which terminates solidification with the formation of eutectic-like constituents. Also note the presence of these secondary constituents (arrows) at interdendritic regions scattered throughout the microstructures.

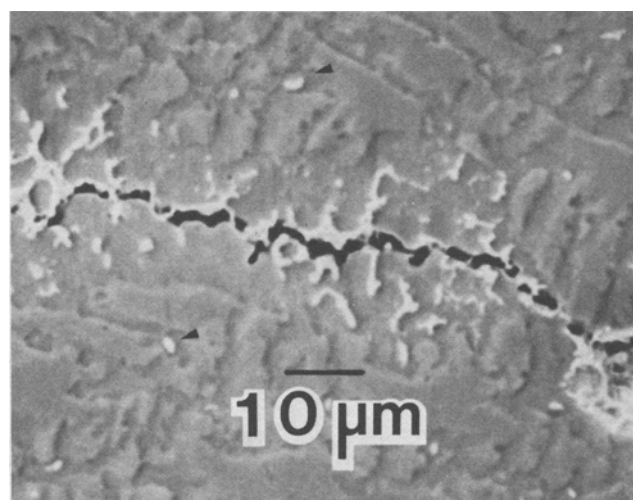
Thin foil micrographs and EDS spectra from minor phases found in the various weld metals are shown in Figures 11 through 13. Figure 11(a) shows the structure found in Alloy C-4 weld metal. The dendritic-shaped second



(a)

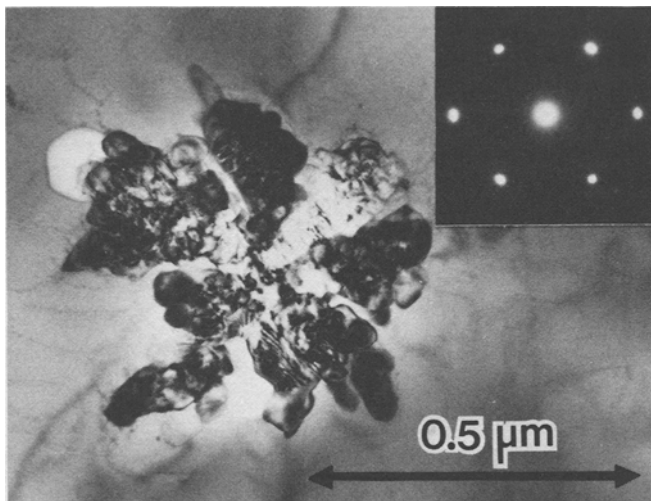


(b)

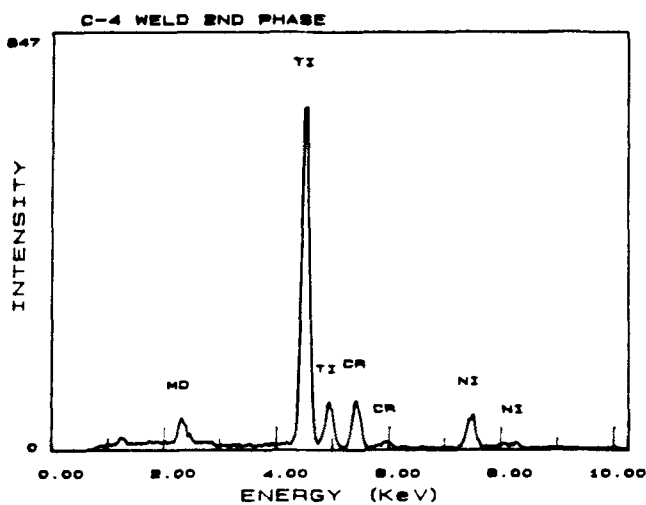


(c)

Fig. 10—Secondary electron micrographs of hot-cracked regions in (a) Alloy C-4, (b) Alloy C-22, and (c) Alloy C-276; all specimens etched in 10 pct chromic acid.



(a)



(b)

Fig. 11—(a) Thin foil electron micrograph of TiC, [110] zone, found in Alloy C-4 weld metal; (b) EDS spectrum.

phase was indexed to TiC (fcc,  $a_0 = 0.427$  nm). This was the only minor phase found in Alloy C-4 by thin foil analysis. Figure 11(b) is the EDS spectrum obtained from this phase and it clearly shows the high Ti concentration expected in TiC.

Figures 12(a) through (c) are thin foil micrographs of the minor phases found in Alloy C-22. Three topologically-close-packed (TCP) intermetallics were observed in this system:  $\sigma$  (tetragonal,  $a = b = 0.908$  nm,  $c = 0.475$  nm),  $P$  (orthorhombic,  $a = 0.907$  nm,  $b = 1.698$  nm,  $c = 0.475$  nm), and  $\mu$  (hexagonal,  $a = 0.476$  nm,  $c = 2.591$  nm). Figure 12(d) shows the EDS spectra from the three minor phases. Note the similarity in composition. In addition to large amounts of Ni, Cr, and Mo, smaller amounts of W, Fe, Co, and P can be seen in each phase. It was observed that approximately 80 pct of the total minor constituent population was  $P$ , approximately 20 pct was  $\sigma$ , and only a trace amount was  $\mu$ .

Figures 13(a) and 13(b) are thin foil micrographs of the minor phases found in Alloy C-276. Two topologically-close-packed intermetallics were observed,  $P$  and  $\mu$ , in

approximately equal amounts. The EDS spectra from these two phases are shown in Figure 13(c). These are qualitatively similar to those seen in Figure 12(d) except for generally less intense Cr peaks.

Phase chemistries were determined for the  $\gamma$  matrix and for all of the TCP phases found in weld metal from Alloys C-22 and C-276, using the AEM procedure outlined above. Table III gives the results of these analyses. As can be seen, all of the TCP phases are enriched in Mo and W and depleted in Ni and Fe relative to the  $\gamma$  matrix. The Cr contents of the TCP phases are similar to those of the matrix, and there is no apparent Co partitioning to the TCP phases. There appears to be a somewhat higher Mo content in the TCP phases of Alloy C-276 when compared to those in Alloy C-22. The Cr contents of the TCP phases in Alloy C-276 are less than those of the TCP phases in Alloy C-22. These observations correlate with bulk chemistries in that Alloy C-276 contains more Mo and less Cr than Alloy C-22.

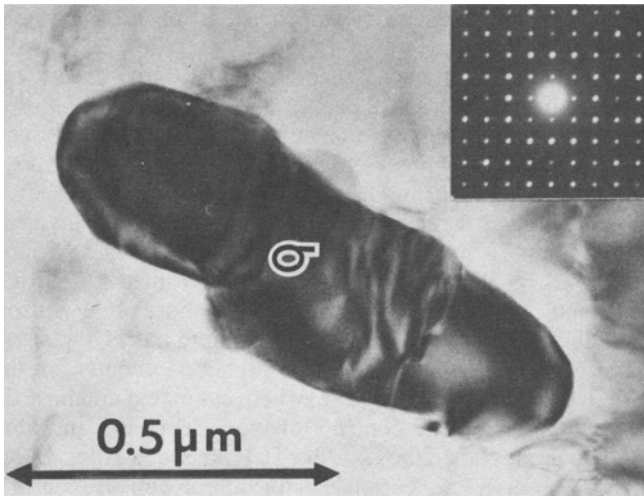
#### IV. DISCUSSION

The welding metallurgy of these alloys can best be understood by referring to known isothermal sections of the phase diagrams for the ternary system, Ni-Cr-Mo, from which these alloys are derived. Figure 14, developed by Raghavan *et al.*<sup>13</sup> and Bloom and Grant,<sup>12</sup> shows isothermal sections at 1250 °C and 850 °C. A solidus diagram is not available, nor is a true liquidus diagram. Bloom and Grant<sup>12</sup> measured the liquidus temperatures for the Ni-Cr-Mo system, and proposed a series of possible reactions between 1250 °C and the liquidus. In the composition range corresponding to the alloys under investigation at the present time, the proposed equilibrium phases are liquid,  $\gamma$ ,  $P$ , and  $\sigma$ .

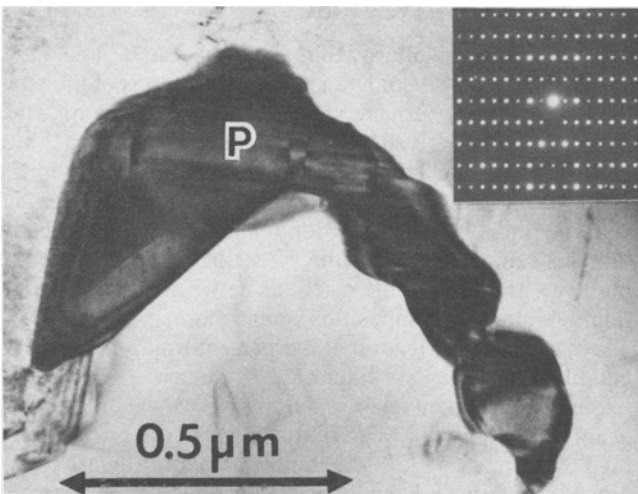
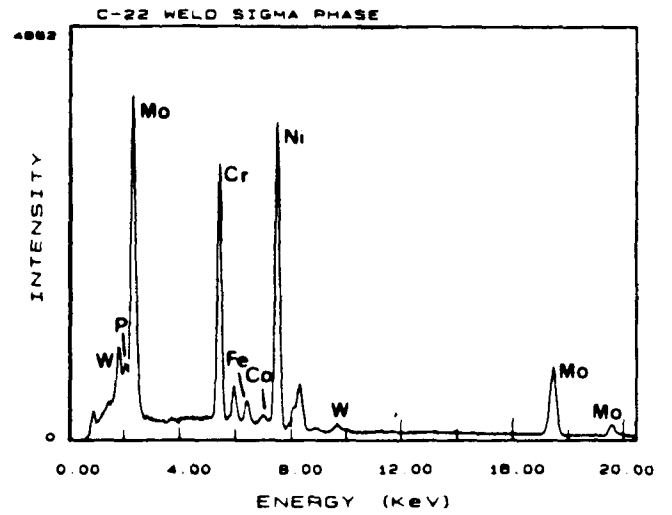
Several important phase relationships can be discerned by examining Figure 14. The first is that  $\mu$  is not present as a high temperature (1250 °C) equilibrium constituent. The regions of stability of the TCP phases (neglecting  $\delta$ , which does not play a role in the present study) are composition dependent.  $\sigma$  is stabilized relative to  $P$  by increasing the Cr concentration. The same relationship can be seen for  $P$  relative to  $\mu$ .  $\mu$  is stabilized relative to  $P$  by increasing the Mo concentration. The same relationship is true for  $P$  relative to  $\sigma$ .

The phase boundaries move as a function of temperature. On cooling from 1250 °C to 850 °C, both the  $\gamma + P$  and the  $\gamma + \sigma$  phase fields are displaced to regions of higher Cr content as the  $\mu + \gamma$  field appears at lower Cr and higher Mo concentrations. The sequence of possible solid state phase transformations important to this study can be visualized by referring to the points labeled 1 through 3 in Figure 14. The composition corresponding to Point 1 exists in the  $P + \gamma$  field at 1250 °C. Upon cooling to 850 °C, this composition is now in the  $\mu + \gamma$  field, necessitating the transformation  $P \rightarrow \mu$  over that temperature range. The composition corresponding to Point 2 exists in the  $\sigma + \gamma$  field at 1250 °C. Upon cooling to 850 °C, this composition now exists in the  $P + \gamma$  field, requiring the transformation  $\sigma \rightarrow P$  over that temperature range.

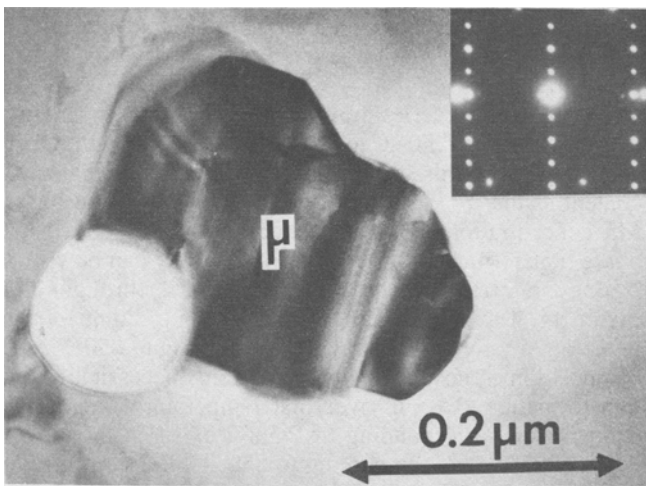
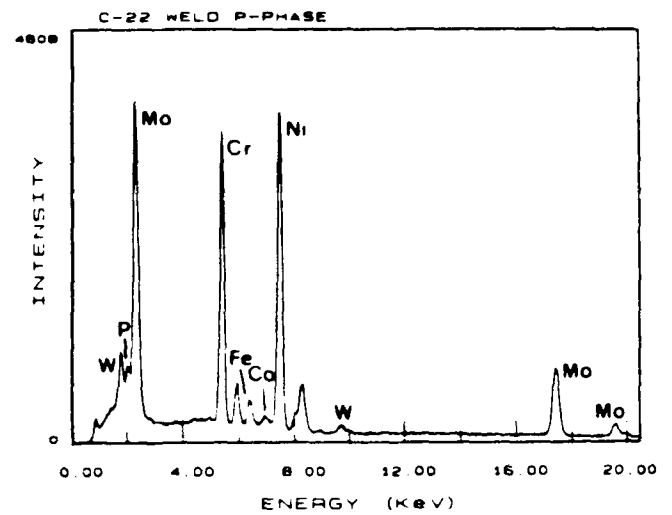
An even more complex transformation sequence can be described for the composition corresponding to Point 3. At 1250 °C, this composition resides in the  $\sigma + \gamma$  field. At 850 °C, it exists in the  $\mu + \gamma$  field. At some temperature



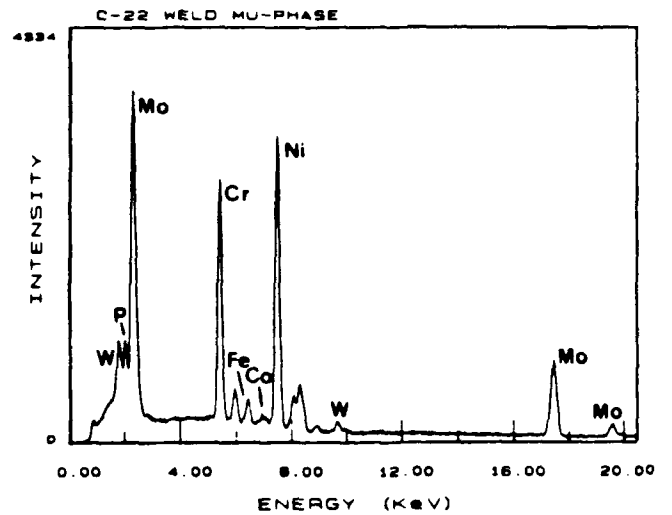
(a)



(b)

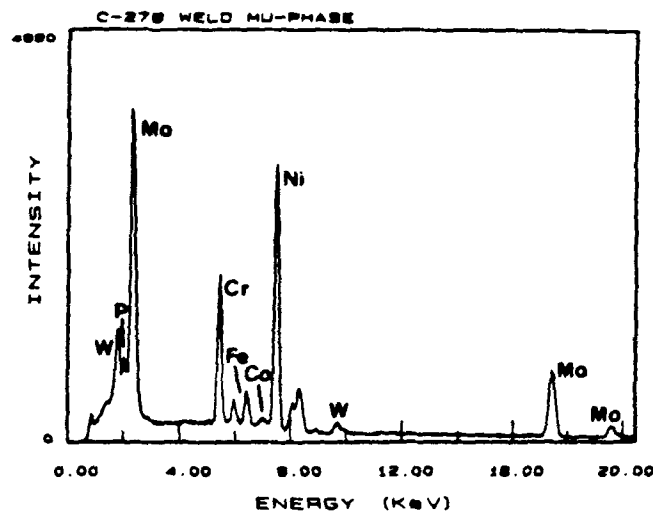
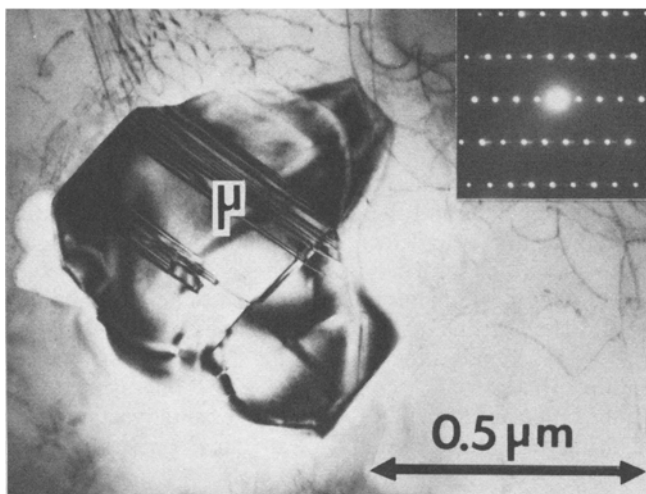
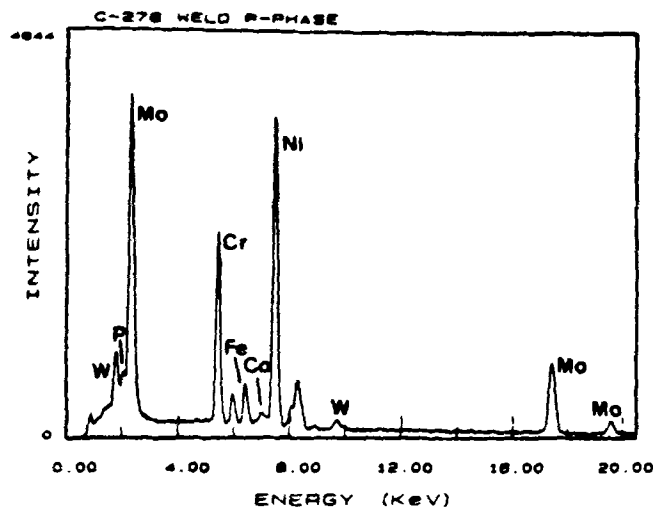
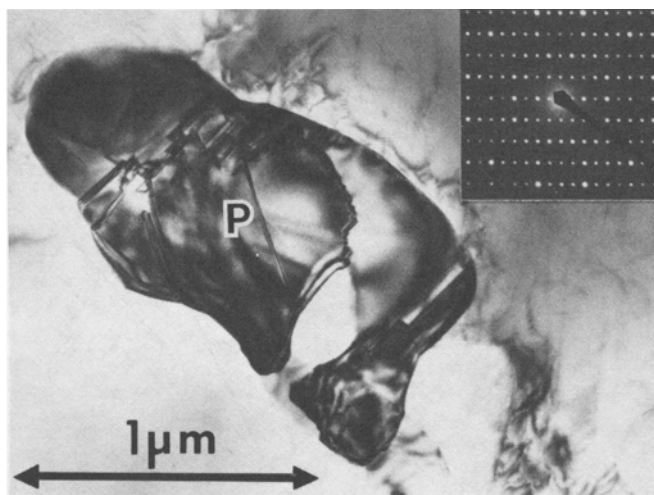


(c)



(d)

Fig. 12—Thin foil electron micrographs of (a)  $\sigma$ , [001] zone, (b) P, [001] zone, and (c)  $\mu$ , [1 $\bar{1}$ 00] zone in Alloy C-22 weld metal; (d) EDS spectra from the three phases.



(b)

(c)

Fig. 13—Thin foil electron micrographs of (a)  $P$ , [001] zone, and (b)  $\mu$ ,  $[1\bar{2}10]$  zone in Alloy C-276 weld metal; (c) EDS spectra from the two phases.

between 1250 °C and 850 °C, this composition would have to pass through a region where  $P$  was one of the stable phases. This suggests the following transformation sequence on cooling from 1250 °C to 850 °C:  $\sigma \rightarrow P \rightarrow \mu$ .

Prediction of the solidification and solid state transformation sequences in the commercial alloys under study is complicated by the fact that they are not pure ternary (Ni-Cr-Mo) systems. A composition model is proposed to treat the remaining minor alloying elements, especially Fe and W, as equivalents of certain of the major alloying elements (Ni, Cr, Mo). This proposal is analogous to the Cr and Ni equivalent concept<sup>28,29</sup> for predicting the solidification mode<sup>30</sup> and room temperature phase stability<sup>28,29</sup> in austenitic stainless steel weld metal.

First, it is proposed to combine the Mo and W weight fractions to create a Mo equivalent,  $Mo_{eq}$ . By referring to Table III, the similarity in partitioning of Mo and W between the TCP phases and the  $\gamma$  matrix is obvious. Both elements partition preferentially to the TCP phases. This is in agreement with the observations of Raghavan *et al.*<sup>5</sup> for  $P$  and  $\mu$  formation during high-temperature heat treatments of Alloy C-276.

A more subtle similarity in behavior among Mo and W can be seen by examining the Mo and W compositional data for Alloy C-22, in which all three TCP phases are present simultaneously. The average Mo concentration of the TCP phases increases in the order:  $\sigma$ ,  $P$ ,  $\mu$ , as would be predicted from the phase diagrams of Figure 14. The average W concentration in the TCP phases increases in the same order, mimicking the behavior of Mo. A similarity in the chemical behavior (partitioning and phase stabilization) among Mo and W is not surprising. The refractory nature and body-centered-cubic crystal structure of both elements suggests similarities in bonding characteristics and hence chemical properties.

Second, it is proposed to combine the Fe and Ni weight fractions to create a Ni equivalent,  $Ni_{eq}$ . Again, by referring to Table III, the similarity in partitioning behavior of Ni and Fe is obvious. Both elements remain preferentially in the  $\gamma$  matrix. Within most of the high temperature region under consideration, both Ni and Fe have face-centered-cubic (fcc) crystal structures, and so their partitioning to the fcc- $\gamma$  matrix is also not surprising. The similarity in partitioning behavior among Ni and Fe can be seen in more subtle detail

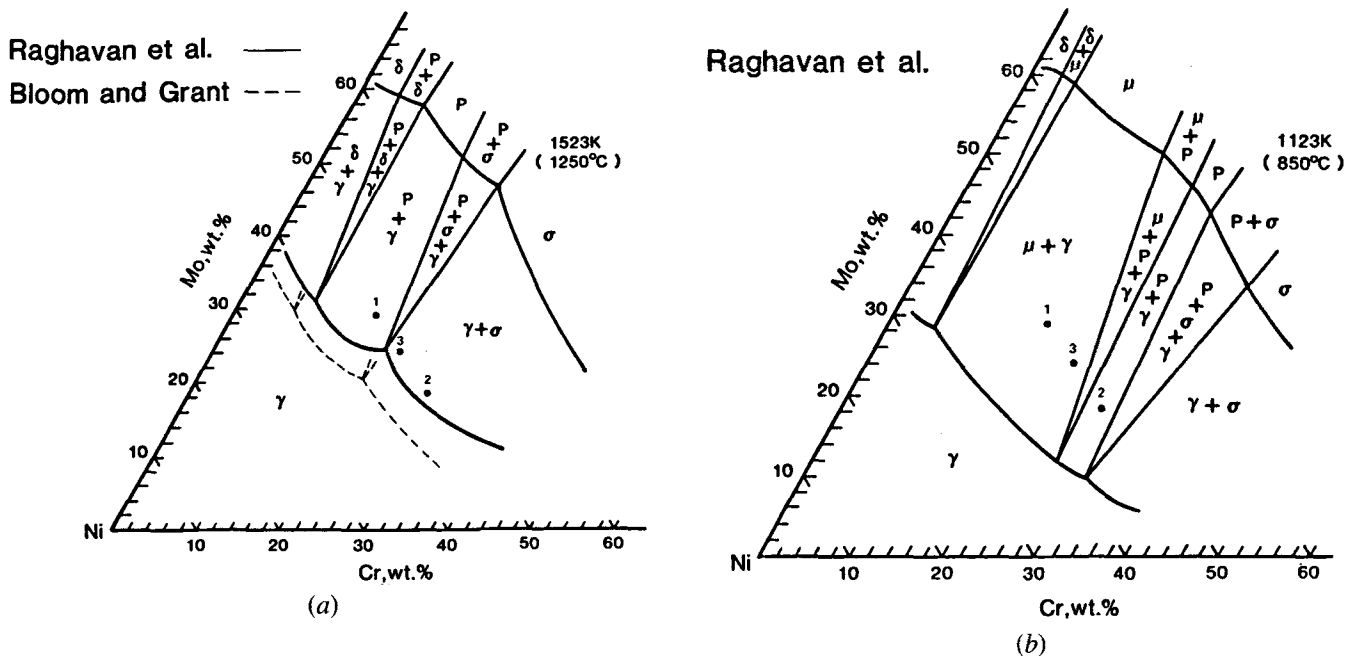


Fig. 14—(a) 1250 °C isothermal section of the Ni-Cr-Mo system; (b) 850 °C section; points 1, 2, and 3 described in text.

by examining the partition ratios: wt pct  $Fe_{TCP}/wt$  pct  $Fe_{\gamma}$ , and wt pct  $Ni_{TCP}/wt$  pct  $Ni_{\gamma}$ . When the Fe and Ni concentrations are each averaged among all of the TCP phases within a single alloy and ratioed against the concentration of these two elements in the residual matrix, a value of approximately 0.6 is obtained for both elements in both Alloys C-22 and C-276.

Third, it is also proposed that the remainder of the minor alloying elements combine with Ni and Fe as part of the  $Ni_{eq}$ . In the present study, Co was found in essentially equal quantities in all phases, suggesting that it is relatively inert. Earlier AEM work by Raghavan *et al.*<sup>5</sup> indicated that Co remains in the  $\gamma$  matrix and does not partition preferentially to the TCP phases. The Co content of the Alloy C-276 in

the earlier study<sup>5</sup> was greater than twice that of the present investigation and therefore differences in composition would be simpler to detect. This earlier result, though, supports the grouping of Co in the  $Ni_{eq}$ .

No alloying elements were observed to behave similarly to Cr. The Cr contents of the TCP phases were observed to follow the trends predicted by the Ni-Cr-Mo phase diagrams. That is, the Cr content of the TCP phases increased in the order:  $\mu$ ,  $P$ ,  $\sigma$ . This result is in qualitative agreement with the earlier AEM study<sup>5</sup> of  $\mu$  and  $P$  phases in Alloy C-276.

In summary, the proposed equivalent composition model is as follows:

$$Mo_{eq} = wt \text{ pct Mo} + wt \text{ pct W} \quad [3]$$

Table III. Phase Compositions (Wt Pct)

Phase	Ni	Mo	Cr	W	Fe	Co
C-22						
$\mu$	33.1 (2.4)*	38.7 (0.2)	19.3 (0.7)	6.3 (1.1)	2.1 (0.2)	0.6 (0.2)
$P$	32.6 (0.8)	37.4 (1.0)	21.7 (0.7)	5.3 (1.1)	2.2 (0.2)	0.9 (0.4)
$\sigma$	34.5 (0.6)	34.9 (0.4)	23.4 (1.3)	4.2 (1.2)	2.2 (0.1)	0.9 (0.2)
$\gamma$	58.5 (1.2)	12.7 (0.8)	21.6 (0.5)	2.9 (0.7)	3.4 (0.1)	0.9 (0.2)
Nom	56.96	13.43	21.22	3.29	3.17	0.84
C-276						
$\mu$	33.2 (0.8)	40.9 (0.6)	15.2 (0.9)	6.2 (1.6)	3.5 (0.3)	1.0 (0.5)
$P$	33.5 (0.6)	39.7 (1.5)	15.7 (0.6)	6.5 (1.6)	3.7 (0.2)	0.8 (0.4)
$\gamma$	57.0 (2.3)	16.0 (1.9)	16.3 (0.4)	4.2 (0.8)	5.6 (0.3)	1.0 (0.3)
Nom	55.58	15.56	15.83	3.93	5.44	0.96

\*Values in parentheses equal 1 standard deviation.

$$\text{Cr}_{\text{eq}} = \text{wt pct Cr} \quad [4]$$

$$\text{Ni}_{\text{eq}} = \text{wt pct Ni} + \text{wt pct Fe} + \sum \text{wt pct X}_i \quad [5]$$

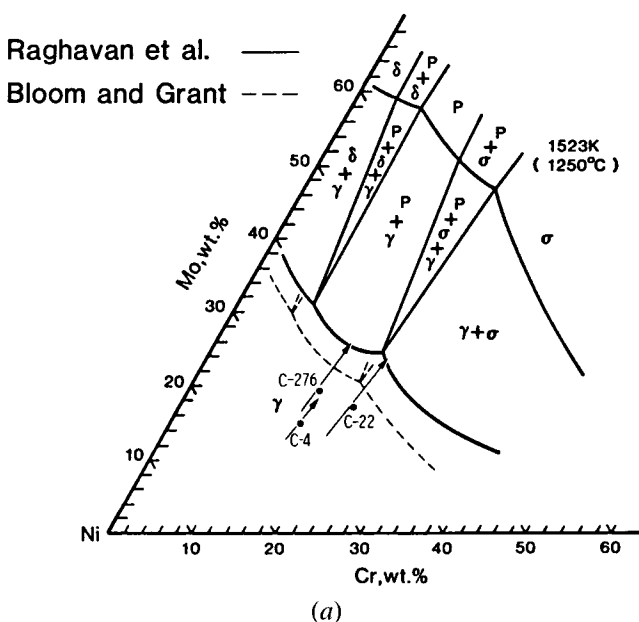
where  $\sum \text{wt pct X}_i$  is the total remaining alloy content not included in the other equivalents. Unlike the case with austenitic stainless steel weld metal Ni and Cr equivalents,<sup>28,29</sup> no "weighting factors" are included in the equivalents defined here. It was felt that the data base was not extensive enough to attempt to determine appropriate weighting factors. Using the definitions given above to establish an "equivalent" composition for the alloys under study, the sequence of phase transformations leading to the observed room temperature microstructure will be described.

Table IV gives the nominal equivalent compositions for the three alloys under study. These compositions are plotted on the Ni-Cr-Mo isothermal sections in Figure 15. In addition to the nominal compositions, the segregation profiles resulting from solidification, in equivalent terms, are shown as the arrows associated with each nominal composition. The tail of each arrow represents the composition of the initial solid to crystallize from the melt, the dendrite core region. The head of the arrow represents the final solidification composition, that of the interdendritic regions. Although all of the bulk equivalent compositions lie within the single phase  $\gamma$  field at 1250 °C, irrespective of the diagram used, solidification segregation results in the final solidification compositions for Alloys C-22 and C-276 being located within fields of TCP phase stability.

Table IV. Equivalent Compositions\*

Equivalent	HASTELLOY C-4	HASTELLOY C-22	HASTELLOY C-276
Cr	15.69	21.22	15.83
Ni	69.25	62.06	64.68
Mo	15.06	16.72	19.49

\*All values in weight percent.



An experimentally determined solidus section is not available for this system. Kaufman and Nestor<sup>31</sup> calculated the 1277 °C and 1227 °C sections of the Ni-Cr-Mo system. Although neither diagram contained the experimentally confirmed  $P$  phase, the 1277 °C section contained liquid phase in equilibrium with a TCP phase ( $\sigma$ ). Bloom and Grant<sup>12</sup> indicated that the minimum solidus temperature in the Ni-Cr-Mo system was approximately 1275 °C. These data suggest that the experimentally determined 1250 °C section is quite close to the solidus. This further implies that the phases present in the 1250 °C section are those present at the termination of solidification. Assuming that the presence of the minor alloying elements does not change the phase diagrams much, the 1250 °C section can be used, along with the experimentally determined segregation profiles to predict the solidification microstructure of the alloys under study. The 850 °C section can be used to predict subsequent solid state transformations.

For Alloy C-4, solidification begins and ends within the single phase  $\gamma$  region. There is not sufficient segregation of Mo and Ni to allow this alloy to enter into any  $\gamma + \text{TCP}$  phase field. TEM analysis revealed the presence of widely dispersed TiC in the weld microstructure. Microprobe analysis showed that Ti does segregate to interdendritic regions, and solidification can terminate locally with the formation of this phase. Lippold<sup>32</sup> identified a TiC constituent in Alloy 800 weld metal that is morphologically identical to the TiC particle shown in Figure 11(a). The TiC in that study was also an interdendritic, terminal solidification constituent. The very low volume fraction of this constituent in Alloy C-4 is such that its formation is not discernible in the DTA profiles.

Solidification of Alloy C-276 begins with the crystallization of  $\gamma$ , but ends with the terminal solidification of  $P$  phase as the solidification path is such that it enters the region of  $\gamma + P$  stability (Figure 15(a)). The DTA curve (Figure 4(c)) shows the presence of a secondary solidi-

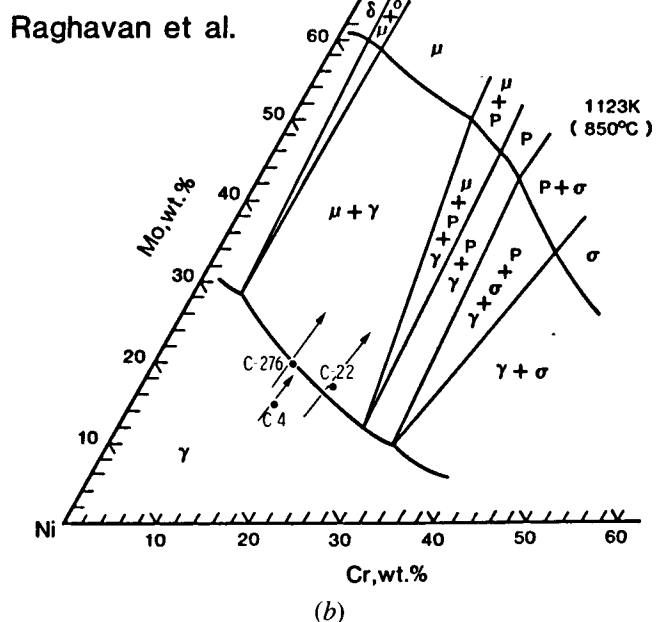


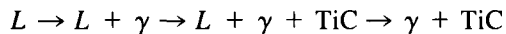
Fig. 15— Isothermal sections: (a) 1250 °C, (b) 850 °C, showing nominal equivalent compositions and equivalent solidification profiles (arrows).

fication peak at approximately 1285 °C. This peak corresponds to the crystallization of  $P$  phase and it occurs at a temperature in good agreement with those suggested earlier.<sup>12,31</sup> As the solidified weld metal cools, it enters the region of  $\gamma + \mu$  stability (Figure 15(b)) which results in at least partial transformation of  $P$  to  $\mu$ . As in many weld metal transformations, sufficient time at temperature is not available for completion of the  $P \rightarrow \mu$  reaction. The weld metal microstructure is then composed of intermediate ( $P$ ) and final ( $\mu$ ) transformation products in a  $\gamma$  matrix. Figure 16 is a TEM micrograph showing the possible growth of  $\mu$  on  $P$  in Alloy C-276 weld metal. The equivalent composition model used in conjunction with the ternary phase diagrams precludes the formation of  $\sigma$  in Alloy C-276 because of its relatively low  $Cr_{eq}$ .

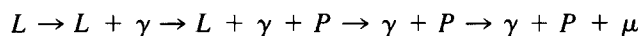
Solidification of Alloy C-22 also begins with the primary crystallization of  $\gamma$ , but this time terminates with the formation of  $\sigma$  phase (Figure 15(a)). The higher  $Cr_{eq}$  of this alloy is such that  $\sigma$  forms in preference to  $P$ . The DTA profile (Figure 4(b)) reveals a secondary solidification event, also in the range of 1285 °C, this being the crystallization of  $\sigma$ . Subsequent solid state transformation of  $\sigma$  involves a two-step process of  $\sigma \rightarrow P$  and  $P \rightarrow \mu$ , in a manner analogous to that described for Point 3, Figure 14. In this case, assuming neither solid state transformation goes to completion, the final weld metal microstructure will consist of  $\gamma$  plus all three TCP phases:  $\sigma$ ,  $P$ , and  $\mu$ .

In summary, the proposed sequences of transformation in the alloys studied are given as follows:

C-4



C-276



C-22

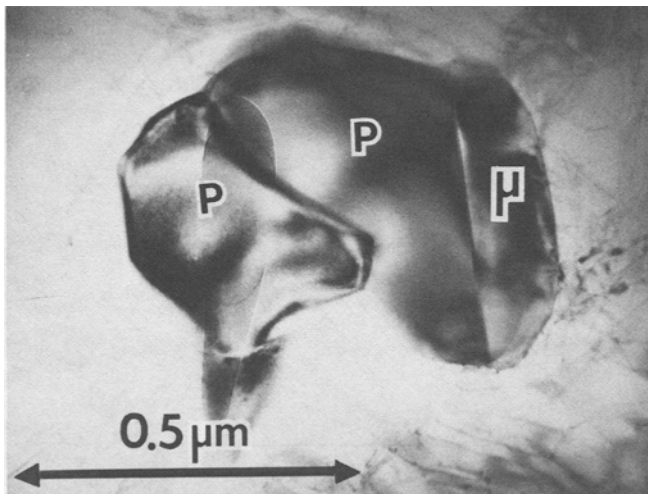
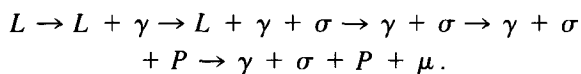


Fig. 16—Thin foil electron micrograph showing growth of  $\mu$  on  $P$  in Alloy C-276 weld metal.

Although the weld metal hot-cracking resistance of each alloy was very good, the resistance of Alloy C-4 was the best. This can be attributed to the lack of a TCP terminal solidification constituent. The formation of a TCP constituent accompanies an extension of the solidification temperature range, a situation less desirable from a hot-cracking standpoint. This extension of the solidification temperature range can be seen indirectly in Figure 3. Both Alloys C-22 and C-276 have maximum crack length values greater than those of Alloy C-4 ( $\approx 0.40$  mm vs  $\approx 0.15$  mm). The similarity in maximum crack length data among Alloys C-22 and C-276 can be understood by reviewing the DTA data of Figures 4(b) and 4(c). Both alloys have very similar curves including temperature range from initiation of solidification to termination of solidification with TCP phase formation. The greater cracking susceptibility of Alloy C-276 can be related to the amount of TCP phase formed (which is also proportional to the amount of liquid phase remaining at 1285 °C) at the termination of solidification. The size of the DTA TCP phase solidification peak was greater for Alloy C-276 than for Alloy C-22. Assuming similar heats of fusion for  $\sigma$  and  $P$  phases (they have similar chemical compositions and both are topologically close packed), this implies a larger amount of residual liquid present in Alloy C-276. According to Borland,<sup>33</sup> this would increase the susceptibility to hot cracking.

## V. CONCLUSIONS

1. Among the HASTELLOY C-type alloys examined, a resistance to hot-cracking ranking can be given as follows: C-4 > C-22 > C-276. All alloys would be expected to be readily weldable in most situations.
2. Alloys C-22 and C-276 terminate solidification with the formation of a TCP constituent; Alloy C-4 does not.
3. The following equivalent composition model is proposed to account for the behavior of the minor elements (W, Fe, etc.) in these alloys:

$$Mo_{eq} = \text{wt pct Mo} + \text{wt pct W}$$

$$Cr_{eq} = \text{wt pct Cr}$$

$$Ni_{eq} = \text{wt pct Ni} + \text{wt pct Fe} + \sum \text{wt pct } X_i,$$

where  $\sum \text{wt pct } X_i$  is the total remaining alloy content not included in the other equivalents.

4. The equivalent composition model used in conjunction with available Ni-Cr-Mo phase diagrams correctly predicts the sequence of transformations in the alloys studied (except for the formation of TiC in Alloy C-4).

## ACKNOWLEDGMENTS

The authors would like to acknowledge the assistance of Ellen Semarge in performing the microprobe analysis and William Hammett for doing the DTA experiments. This work was performed at Sandia National Laboratories, Albuquerque, New Mexico, and was supported by the United States Department of Energy under contract number DE-AC04-76DP00789.

## REFERENCES

1. S. J. Matthews: *Superalloys 1976*, pp. 215-26.
2. H. M. Tawancy, R. B. Herchenroeder, and A. I. Asphahani: *Jour. of Metals*, 1983, vol. 35, No. 6, pp. 37-43.
3. N. Sridhar, J. B. C. Wu, and P. E. Manning: *Jour. of Metals*, 1985, vol. 37, No. 11, pp. 51-53.
4. H. M. Tawancy: *Metall. Trans. A*, 1980, vol. 11A, pp. 1764-65.
5. M. Raghavan, B. J. Berkowitz, and J. C. Scanlon: *Metall. Trans. A*, 1982, vol. 13A, pp. 979-84.
6. F. G. Hodge and R. W. Kirchner: *Corrosion*, Aug. 1976, pp. 332-36.
7. F. G. Hodge: *Corrosion*, Oct. 1973, pp. 375-83.
8. R. B. Leonard: *Corrosion*, May 1969, pp. 222-28.
9. W. A. Owczarski: *Physical Metallurgy of Metal Joining*, TMS/AIME Pub., R. Kossowsky and M. E. Glicksman, eds., June 1980, pp. 166-89.
10. M. J. Cieslak, A. D. Romig, Jr., and T. J. Headley: *Microbeam Analysis 1985*, pp. 179-88.
11. S. Rideout, W. D. Manly, E. L. Kamen, B. S. Lement, and P. A. Beck: *Trans. AIME*, Oct. 1951, pp. 872-76.
12. D. S. Bloom and N. J. Grant: *Trans. AIME*, Feb. 1954, pp. 261-68.
13. M. Raghavan, R. R. Mueller, G. A. Vaughn, and S. Floreen: *Metall. Trans. A*, 1984, vol. 15A, pp. 783-92.
14. W. F. Savage and C. D. Lundin: *Welding Journal*, Oct. 1965, pp. 433-s-42-s.
15. W. F. Savage and C. D. Lundin: *Welding Journal*, Nov. 1966, pp. 497-s-503-s.
16. A. C. Lingenfelter: *Welding Journal*, Sept. 1972, pp. 430-s-36-s.
17. *Methods of High Alloy Weldability Evaluation*, WRC Pub., Nov. 1970.
18. Y. Arata, F. Matsuda, and S. Katayama: *Trans. of JWRI*, Dec. 1976, vol. 5(2), pp. 35-51.
19. M. J. Cieslak: Ph.D. Thesis, "Fundamental Metallurgical Investigations of Alloy CN-7M Weldments," Rensselaer Polytechnic Institute, Troy, NY, May 1983.
20. G. F. Bastin, H. J. M. Heijligers, and F. J. J. van Loo: *X-ray Spec.* 13: 91, 1984.
21. A. D. Romig, Jr.: Sandia National Laboratories Report SAND82-2938, 1983.
22. J. I. Goldstein, J. L. Costley, G. W. Lorimer, and S. J. B. Reed: *SEM/1977*, pp. 315-24.
23. M. J. Cieslak, T. J. Headley, and A. D. Romig, Jr.: Sandia National Laboratories, Albuquerque, NM, unpublished research, 1985.
24. G. A. Knorovsky and T. J. Headley: Sandia National Laboratories, Albuquerque, NM, unpublished research, 1985.
25. J. A. Brooks, A. W. Thompson, and J. C. Williams: *Physical Metallurgy of Metal Joining*, R. Kossowsky and M. E. Glicksman, eds., TMS/AIME Pub., June 1980, pp. 117-36.
26. R. A. Patterson and J. O. Milewski: *Welding Journal*, Aug. 1985, pp. 227-s-31-s.
27. M. J. Cieslak and W. F. Savage: ASTM STP 756, *Stainless Steel Castings*, pp. 241-58.
28. A. L. Schaeffer: *Metal Progress*, 1949, vol. 56, No. 11, pp. 680-80B.
29. C. J. Long and W. T. DeLong: *Welding Journal*, July 1973, pp. 281-s-97-s.
30. N. Suutala and T. Moiso: *Solidification Technology in the Foundry and Casthouse*, The Metals Society, University of Warwick, Coventry, 15-17 Sept., 1980, Session IVa, pp. 1-10.
31. L. Kaufman and H. Nestor: *Metall. Trans.*, 1974, vol. 5, pp. 1617-21.
32. J. C. Lippold: *Welding Journal*, March 1984, pp. 91-s-103-s.
33. J. C. Borland: *British Welding Journal*, Aug. 1960, pp. 508-12.